Load Independent Constant Current Wireless Charger Using Hybrid Topology and Integrated Reverse-Coupled Compensators

Armin Gheysari, *Student Member, IEEE*, Ali Yazdian Varjani, *Member, IEEE*, and Amir Babaki, *Member, IEEE*

***Abstract*—Inductive power transfer (IPT) technology is well-suited for wireless charging of electric vehicles due to its convenience, inherent safety, and resilience to weather conditions. Maintaining a constant output current across varying coupling coefficients and load resistances is a critical feature of IPT systems. This article proposes a dual-switch hybrid *LCC*-S inverter with a novel topology featuring reverse-coupled primary and secondary compensation coils integrated into a new dual D-quadrature-dual D magnetic coupler. This design eliminates cross-circuit mutual inductance and enhances system stability under mismatched conditions. The proposed two-switch topology replaces the conventional full-bridge inverter, eliminating ac switches in the resonance network and the need for an active rectifier on the receiver side, thereby reducing losses, component count, gate drive circuits, and additional control signals. By relocating inductors from the printed circuit board (PCB) to the magnetic couplers, the PCB size is significantly reduced, while the obtained tolerant system eliminates the need for complex control methods. A 1 kW prototype operating in zero voltage switching mode has been designed and tested, achieving output current regulation with less than 9% deviation across varying load and coupling conditions, with system efficiency maintained between 88% and 92% .**

***Index Terms*—Electromagnetic coupling, inductive energy storage, zero voltage switching (ZVS).**

I. Introduction

SINCE Nikola Tesla proposed the wireless power transfer (WPT) system in 1914, technology has rapidly advanced, particularly inductive power transfer (IPT), known for its high efficiency in mid-range power applications [1]. IPT systems wirelessly transmit power through an air gap between magnetic couplers, aiming to replace plug-in charging with wireless options due to advantages like safety, reliability, and environmental adaptability [2] and [3]. The absence of physical connections makes IPT suitable for various applications requiring batteries [4], such as biomedical implants [5], electric vehicles (EVs) [6], and household appliances [7]. An effective IPT system must withstand varying airgap s and regulate output parameters like voltage and current across varying load resistances [8]. This ensures a constant output current despite changes in air gap and power demand [9], [10]. Achieving nearly constant current (CC) or constant voltage (CV) charging necessitates closed-loop control during battery charging [11]. However, increased varying airgap tolerance and load variation can hinder zero-voltage switching (ZVS) and zero-phase angle (ZPA) conditions [12]. Current methods often incorporate controllable dc–dc converters on the Secondary side [13], [14], [15], [16], complicating control circuitry and affecting reliability as well as efficiency. Additionally, dc–dc converters have performance limitations across varying output loads due to restricted duty cycle ranges [17].

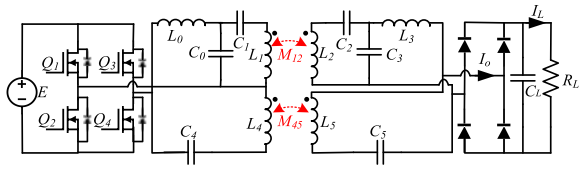

Fig. 1. Circuit proposed in [6].

To address these challenges, existing methods often rely on complex designs, such as additional switches or hybrid topologies, which increase system complexity and cost while offering limited tolerance to significant air gap variations [18], [19], [20], [21]. This underscores the need for a simpler and more robust approach.

In [6], to suppress output current oscillations caused by coupling variations, an *LCC*-S hybrid topology with double D-quadrature (DDQ) magnetic couplers, capable of misalignment tolerance, was proposed for a wireless charging system with constant output current, as illustrated in Fig. 1. However, this article proposes several modifications to further enhance the misalignment tolerance of the system in [6]. For better understanding, the key innovations of this article are highlighted as follows.

1) Proposing reverse coupling between resonance circuits in addition to the coupling between the main magnetic pads in order to obtain constant output current for utilizing CC battery charging independent to load and coupling coefficient changes.

Received 15 January 2025; revised 4 May 2025 and 15 August 2025; accepted 20 September 2025. Date of publication 26 September 2025; date of current version 13 November 2025. Recommended for publication by Associate Editor C. K. Lee. *(Corresponding author: Ali Yazdian Varjani.)*

Armin Gheysari and Ali Yazdian Varjani are with Electrical and Computer Engineering Department, Tarbiat Modares University, Tehran 14115-111, Iran (e-mail: a.gheysari@modares.ac.ir; yazdian@modares.ac.ir).

Amir Babaki is with the Institute of Mechanical and Electrical Engineering, University of Southern Denmark, DK-5230 Odense, Denmark (e-mail: amirbabaki@sdu.dk).

Color versions of one or more figures in this article are available at https://doi.org/10.1109/TPEL.2025.3615122.

Digital Object Identifier 10.1109/TPEL.2025.3615122

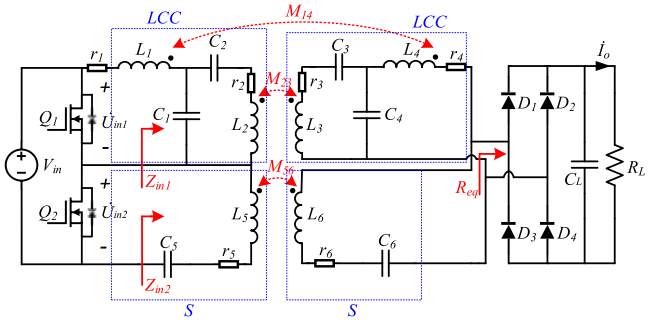

Fig. 2. *LCC*-S hybrid topology system.

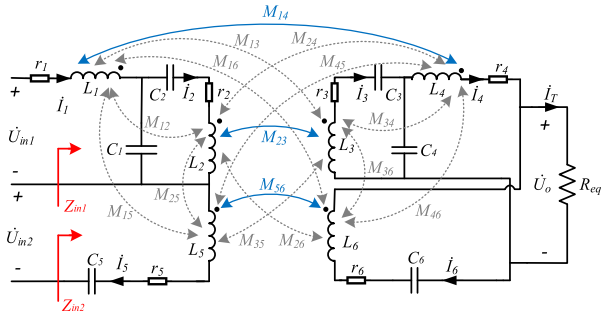

Fig. 3. Equivalent fundamental wave circuit.

2) Integration of the proposed reverse coupling with the main magnetic pads, resulting in simplicity and reduced printed circuit board (PCB) size.
3) Design of a novel dual D-quadrature–dual D (DDQDD) magnetic coupler unlike to typical DDQ configuration to guarantee misalignment tolerant in all directions.
4) Proposal of a two-switch topology providing dual resonance voltages.

Initially, a reverse coupling between the coils L_1 and L_4 (see Fig. 2) was introduced in addition to the previous M_{23} and M_{56} couplings, enhancing output current stability under mismatched conditions. Consequently, a novel DDQDD magnetic coupler was designed to establish three distinct couplings between the transmitter and receiver while eliminating cross-circuit mutual inductance. To simplify the design and reduce losses, a two-switch topology was proposed to provide two separate voltages for the resonance network, replacing the full-bridge inverter in Fig. 1. Providing two separate voltages for the resonance network not only simplifies the control algorithm but also enables output current control in each loop of the hybrid structure. The approach contains no ac switches in the resonance network or active rectifier on the receiver side, thus reducing the number of components. Accordingly, the proposed passive solution for misalignment tolerant saves complex control methods and extra switching converters. Finally, relocating the inductors from the PCB to the magnetic couplers significantly reduces the PCB size.

The rest of this article is organized as follows: Section II examines the proposed LCC-S hybrid topology for maintaining constant output current under varying distances and loads. Section III discusses the designed magnetic couplers, while Section IV presents simulation results. Section V validates the strategy with a 1 kW experimental system. Finally, Section VI concludes the article.

II. Circuit Analysis

The supplementary MOSFETs Q_1 and Q_2 are switched ON/OFF with an equal duty cycle opposite to each other. The proposed circuit topology in Fig. 2 includes V_{in} as the dc power supply, R_L as the load resistance, C_L as the output filter capacitor, and ω as the system operating frequency. In order to maintain a constant output current at different distances and enable magnetic coupler tolerating in a certain amount of varying airgap, magnetic coils must be designed in such a way that only mutual inductances between each winding in primary and the corresponding winding in secondary side, M_{14}, M_{23} and M_{56}, are considerable, while all the rest possible mutual inductances M_{35}, M_{26}, M_{36}, M_{25}, M_{34}, M_{16}, M_{46}, M_{15}, M_{23}, M_{12}, M_{24} and M_{13} are almost zero in a wide range of distances which is shown in Fig. 3. This will be further explained in the magnetic design section. In order to provide the resonance conditions for each side of the entire circuit, all inductors and capacitors should satisfy

$$\begin{cases} \omega^2 L_1 C_1 = \omega^2 L_2 \frac{C_1 C_2}{C_1 + C_2} = 1 \\ \omega^2 L_4 C_4 = \omega^2 L_3 \frac{C_3 C_4}{C_3 + C_4} = 1 \\ \omega^2 L_5 C_5 = \omega^2 L_6 C_6 = 1 \end{cases}. \tag{1}$$

The coupling coefficient between two coils, K_{ij}, is obtained from the following:

$$K_{ij} = \frac{M_{ij}}{\sqrt{L_i L_j}} \tag{2}$$

where M_{ij} is the mutual inductance between two coils L_i and L_j. Equivalent output load resistant reflected to the input side of secondary rectifier, R_{eq}, like the one in Fig. 3 can be calculated as follows:

$$R_{\text{eq}} = \frac{8}{\pi^2} R_L \tag{3}$$

where R_L is actual load resistance as seen in Fig. 2 In order to simplify the analysis process, the leakage resistance of r_1 to r_6 are neglected in this analysis as are not comparable to the load. According to Kirchhoff's law, the impedance matrix of hybrid circuit, Z, can be expressed as

$$Z.\dot{I} = \begin{bmatrix} Z_{11} & Z_{12} & 0 & Z_{14} & 0 & 0 \\ Z_{21} & Z_{22} & Z_{23} & 0 & 0 & 0 \\ 0 & Z_{32} & Z_{33} & Z_{34} & 0 & 0 \\ Z_{41} & 0 & Z_{43} & Z_{44} & 0 & Z_{46} \\ 0 & 0 & 0 & 0 & Z_{55} & Z_{56} \\ 0 & 0 & 0 & Z_{64} & Z_{65} & Z_{66} \end{bmatrix} \cdot \begin{bmatrix} \dot{I}_1 \\ \dot{I}_2 \\ \dot{I}_3 \\ \dot{I}_4 \\ \dot{I}_5 \\ \dot{I}_6 \end{bmatrix} = \begin{bmatrix} \dot{U}_{\text{in1}} \\ 0 \\ 0 \\ 0 \\ \dot{U}_{\text{in2}} \\ 0 \end{bmatrix} \tag{4}$$

where

$$Z_{11} = j\omega L_1 + (j\omega C_1)^{-1}, Z_{12} = -(j\omega C_1)^{-1}, Z_{14} = j\omega M_{14}$$
$$Z_{21} = -(j\omega C_1)^{-1}, Z_{22} = j\omega L_2 + (j\omega C_2)^{-1} + (j\omega C_1)^{-1}$$
$$Z_{23} = -j\omega M_{23}, Z_{32} = -j\omega M_{23},$$
$$Z_{33} = j\omega L_3 + (j\omega C_3)^{-1} + (j\omega C_4)^{-1}, Z_{34} = -(j\omega C_4)^{-1}$$
$$Z_{41} = j\omega M_{14}, Z_{43} = -(j\omega C_4)^{-1}, Z_{44} = j\omega L_4 + (j\omega C_4)^{-1} + \mathrm{R_{eq}}$$
$$Z_{46} = \mathrm{R}_{eq}, Z_{55} = j\omega L_5 + (j\omega C_5)^{-1}, Z_{56} = -j\omega M_{56}, Z_{64} = \mathrm{R_{eq}}$$
$$Z_{65} = -j\omega M_{65}, Z_{66} = j\omega L_6 + (j\omega C_6)^{-1} + \mathrm{R_{eq}}. \quad (5)$$

By solving (4) and (5) the currents are expressed

$$\begin{cases} I_1 = R_{\mathrm{eq}} \left(\frac{U_{\mathrm{in1}} M^2{}_{23}}{\omega^2 (L_1 L_4 + M_{14} M_{23})^2} + \frac{U_{\mathrm{in2}} M_{23}}{\omega^2 M_{56} (L_1 L_4 + M_{14} M_{23})} \right) \\ I_2 = \frac{U_{\mathrm{in1}}}{j\omega L_1} \\ I_3 = R_{\mathrm{eq}} \left(\frac{U_{\mathrm{in1}} M_{23}}{\omega^2 L_1 (L_1 L_4 + M_{14} M_{23})} + \frac{U_{\mathrm{in2}}}{\omega^2 M_{56}} \right) \\ I_4 = \frac{U_{\mathrm{in1}} M_{23}}{j\omega (L_1 L_4 + M_{14} M_{23})} \\ I_5 = R_{\mathrm{eq}} \left(\frac{U_{in1} M_{23}}{\omega^2 M_{56} (L_1 L_4 + M_{14} M_{23})} + \frac{U_{\mathrm{in2}}}{\omega^2 M^2{}_{56}} \right) \\ I_6 = \frac{U_{\mathrm{in2}}}{j\omega M_{56}}. \end{cases} \quad (6)$$

According to (6), the total output current of the inverter can be calculated as

$$I_T = \frac{U_{\mathrm{in1}} M_{23}}{j\omega (L_1 L_4 + M_{14} M_{23})} + \frac{U_{\mathrm{in2}}}{j\omega M_{56}}. \quad (7)$$

According to (7), the output current of the circuit is independent to the load resistance due to the absence of the term R_L in either the numerator or denominator of the equations. Therefore, the circuit output is in the form of CC with a slight deviation. Equation (8) presents the output current as introduced in [6]

$$I_o = \frac{U_{\mathrm{in}} M_{12}}{j\omega L_0 L_3} + \frac{U_{\mathrm{in}}}{j\omega M_{45}}. \quad (8)$$

As observed in the circuit presented in Reference [6], the output current has a direct relationship with M_{12} when the mutual inductance M_{12} varies. Therefore, the output current undergoes significant variations. However, in the proposed circuit, the current output (7) demonstrates a different behavior. Due to the coupling between inductors L_1 and L_4, the term $M_{14} \cdot M_{23}$ appears in the denominator. As a result, when the mutual inductances change, this variation affects both the numerator and the denominator. Consequently, the output current in the proposed circuit exhibits less variation compared to [6] when mutual inductances vary.

Equation (9) demonstrates that the input impedances Z_{in1} and Z_{in2} are purely real, lacking any imaginary components, indicating a resistive impedance that enables the achievement of ZPA. To achieve zero voltage switching (ZVS), the input impedance can be made appropriately inductive by fine-tuning the circuit's capacitors and inductors, such as compensation capacitors or inductances, ensuring the necessary conditions for ZVS

$$Z_{\mathrm{in1}} = \frac{U_{\mathrm{in1}}}{R_{eq} \left(\frac{U_{\mathrm{in1}} M^2{}_{23}}{\omega^2 (L_1 L_4 + M_{14} M_{23})^2} + \frac{U_{\mathrm{in2}} M_{23}}{\omega^2 M_{56} (L_1 L_4 + M_{14} M_{23})} \right)}$$
$$Z_{\mathrm{in2}} = \frac{U_{\mathrm{in2}}}{R_{\mathrm{eq}} \left(\frac{U_{\mathrm{in2}}}{\omega^2 M^2{}_{56}} + \frac{U_{\mathrm{in1}} M_{23}}{\omega^2 M_{56} (L_1 L_4 + M_{14} M_{23})} \right)}. \quad (9)$$

For simplicity, all coil resistances are set equal to r_{eq}, which is close to zero, allowing the output power, P_{out}, power loss, P_L, and circuit efficiency, η, to be derived from (10) as follows:

$$\begin{cases} P_{\mathrm{out}} = (I_4 + I_6)^2 \mathrm{R_{eq}} \\ P_L = r_{\mathrm{eq}} \left(I^2{}_1 + I^2{}_2 + I^2{}_3 + I^2{}_4 + I^2{}_5 + I^2{}_6 \right) \\ \eta = \frac{P_{\mathrm{out}}}{P_{\mathrm{out}} + P_L}. \end{cases} \quad (10)$$

Therefore, by substituting the currents I_1 to I_6 as shown in (6) and R_{eq} as shown in (3), and r_{eq} as the equivalent resistance of each coil in (10), The output power P_{out}, circuit loss P_L, and converter efficiency, η, can be calculated.

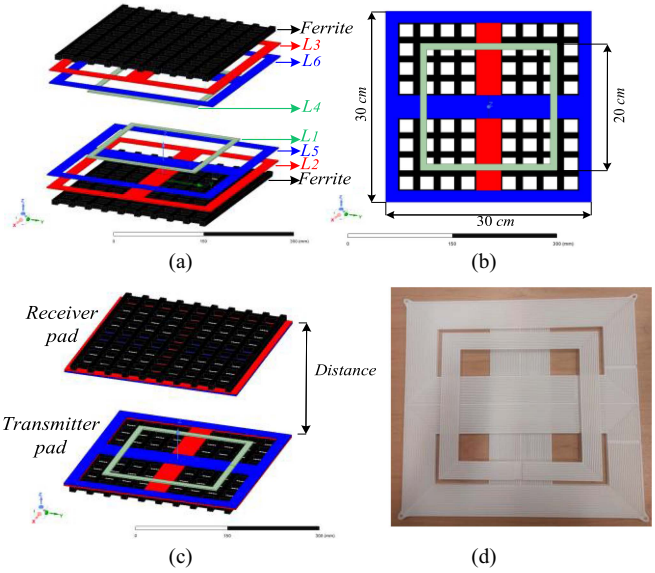

Fig. 4. DDQDD coils' structure. (a) Primary and secondary pad from top view. (b) Both pads from front view (pad size is same for both sides). (c) Assembled pads (all simulated in cubic finite element by Maxwell). (d) 3-D printed DDQDD pads in practice.

III. Design of Magnetic Couplers

The proposed magnetic couplers simulated by 3-D finite element in Ansys-Maxwell shown in Fig. 4 includes a transmitting and receiving coupler, each made of three windings. The aim of the proposed method for pad designing is to meet the figure of merit including constant output current in wider range of varying airgap tolerance and airgaps between the primary and secondary, which can be interpreted to variant coupling coefficient. Coils

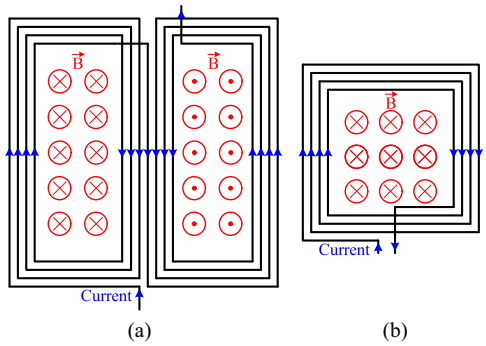

Fig. 5. Wiring configuration of the (a) DD coil and (b) Q coil.

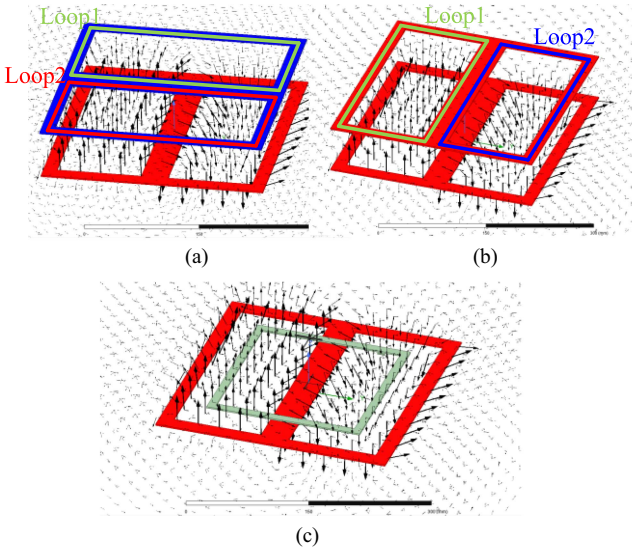

Fig. 6. (a) DD coil versus DD coil with a 90° spatial offset. (b) DD coil versus DD coil with zero angular offset. (c) Q coil versus DD coil.

L_2, L_3, L_5, and L_6 are implemented in form of bipolar double-D (DD) pads with dimension of 30 cm × 30 cm, while coils L_1 and L_4 are shaped as quadrature (Q) pad with dimensions of 20 cm × 20 cm. Ferrite cores also have been mounted on the back of the primary and secondary pads in form of square lattice in order to conduct the linkage flux and reduce leakage flux.

A fundamental principle of magnetic coupling is first illustrated based on Figs. 5 and 6, providing the basis for the subsequent analysis of the mutual inductance values (M). Fig. 5 illustrates the winding configuration of a DD coil [see Fig. 5(a)] and a Q coil [see Fig. 5(b)], with the current flow direction depicted in each. In the DD coil, current flow generates an inward magnetic field on one side and an outward field on the other side, whereas in the Q coil, the magnetic field is oriented in a single direction. As illustrated in Fig. 6(a), two magnetically coils with a 90° spatial offset are presented. The magnetic field, generated by the red DD coil, exhibits an upward direction on one side and a downward direction on the opposite side. The blue DD coil consists of two loops (loop 1 and loop 2). In half of loop 1, the magnetic field points upward, while in the other half, it points downward, resulting in mutual cancellation and thus no induced voltage in loop 1. The same phenomenon occurs in loop 2, where opposing field directions lead to net voltage

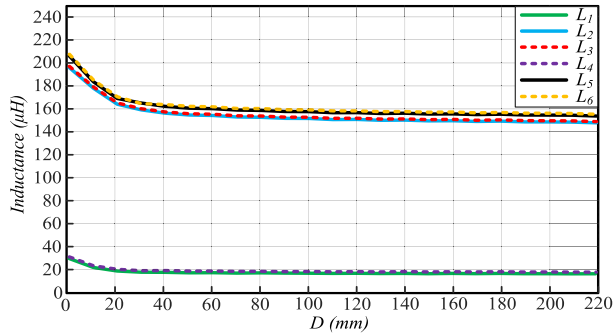

Fig. 7. Self-inductance curves of coils L_1 to L_6 in relation to the distance between the magnetic couplers.

cancellation. Consequently, no voltage is induced in the blue DD coil, and the coupling between the two DD coils remains zero regardless of their separation distance. Two DD coils with zero angular misalignment are shown in Fig. 6(b). The magnetic field generated by the lower DD coil induces an upward-directed field in loop 1 and a downward-directed field in loop 2 of the upper DD coil. Since these loops are connected in series, their induced voltages add up constructively. Thus, the coupling between two DD coils with zero spatial offset is non-zero and varies with the air gap between them. On the other hand, Fig. 6(c) depicts a Q-coil positioned on top of the DD coil. The magnetic field produced by the DD coil exhibits an upward direction in one half of the Q-coil and a downward direction in the other half, leading to mutual cancellation. As a result, the coupling between a DD coil and a Q-coil remains zero, irrespective of their separation distance.

Therefore, in Fig. 4, the coupling between L_2 and L_5/L_6 is zero ($M_{25} = M_{26} = 0$) due to their 90° spatial misalignment. Similarly, L_3 exhibits no coupling with L_5/L_6 for the same reason($M_{35} = M_{36} = 0$). Additionally, L_1 has zero coupling with L_2, L_3, L_5, and L_6 ($M_{12} = M_{13} = M_{15} = M_{16} = 0$). Similarly, L_4 is not magnetically coupled with L_2, L_3, L_5, or L_6 ($M_{24} = M_{34} = M_{45} = M_{46} = 0$) because the magnetic field generated by a DD coil induces opposing flux directions in the two halves of the Q-coil, resulting in mutual cancellation and effectively zero net coupling. Only three coupling pairs remain: L_1-L_4, L_2-L_3, and L_5-L_6, whose coupling coefficients decrease as the air gap between them increases. The variation of the self-inductances L_1 to L_6 in terms of distance between the primary and secondary coupler [see Fig. 4(c)] are shown in Fig. 7. The self-inductance of each coil increases at lower distances due to use of ferrite cores on the other side and its more significant effect on flux conduction path. A significant reduction in self-inductance is observed as the distance between the two coils increases (up to approximately 60 mm), beyond which the inductance values tend to stabilize. As explained in Section II, in order to achieve a constant output current at different air gaps between the magnetic couplers, only the mutual inductances M_{14}, M_{23} and M_{56} should have non-zero values, while the rest of the mutual inductances at all distances should be equal to 0, as illustrated in Fig. 8.

As it can be seen, the distance of 20 mm up to 190 mm between primary and secondary is considered as the operation zone

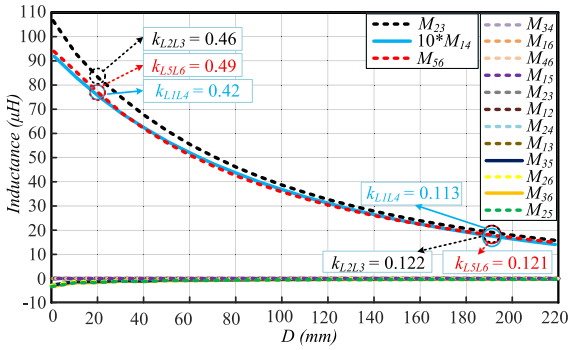

Fig. 8. Mutual inductance curve between windings L_1 to L_6 in relation to the distance between the magnetic couplers.

TABLE I
SYSTEM PARAMETER

Parameter	description	Value
f_s/kHz	Operating frequency	85
$L_1/\mu H$	Primary-side transmitting coil	17.5
$L_2/\mu H$	Primary-side transmitting coil	150
$L_3/\mu H$	Secondary-side transmitting coil	150
$L_4/\mu H$	Secondary-side transmitting coil	17.5
$L_5/\mu H$	Primary-side transmitting coil	156
$L_6/\mu H$	Secondary-side transmitting coil	156
C_1/nF	Primary-side compensation capacitor	206.5
C_2/nF	Primary-side compensation capacitor	25
C_3/nF	Secondary-side compensation capacitor	25
C_4/nF	Secondary-side compensation capacitor	206.5
C_5/nF	Primary-side compensation capacitor	22.5
C_6/nF	Secondary-side compensation capacitor	22.5
C_L/uF	Output filter capacitor	60
Vin/V	Input DC voltage	100
R_L/Ω	Load resistance	4–17
I_o/A	Output current	~8
U_o/V	Output voltage rate	130

and will be more investigated in the following. The maximum effective air gap of the system is 190 mm. Below this range (i.e., below 20 mm), the circuit is heavily inductive and goes out of resonance, while beyond this range (i.e., above 190 mm), the coupling decreases significantly, leading to a reduction in the circuit's output current. Equation (2) represents the coupling coefficient between two windings, showing a direct relationship with the mutual inductance between the windings and an inverse relationship with the self-inductance of the windings. In air gap equal to 20 mm between the magnetic couplers, the coupling coefficient between L_1 and L_4 is $K_{L1L4} = 0.42$, while the coupling coefficient between L_2 and L_3 is $K_{L2L3} = 0.46$ as well as $K_{L5L6} = 0.49$ between L_5 and L_6 windings. Due to the direct relationship with mutual inductance, as the mutual inductance decreases, the coupling coefficient also decreases. Therefore, the coupling coefficient between the windings at a distance of 190 mm is $K_{L1L4} = 0.11$, $K_{L2L3} = 0.12$ and $K_{L5L6} = 0.12$.

IV. SIMULATION RESULTS

In order to validate the design concept of the proposed system, the circuit shown in Fig. 2 has been simulated in the PSpice software. The system parameters are given in Table I.

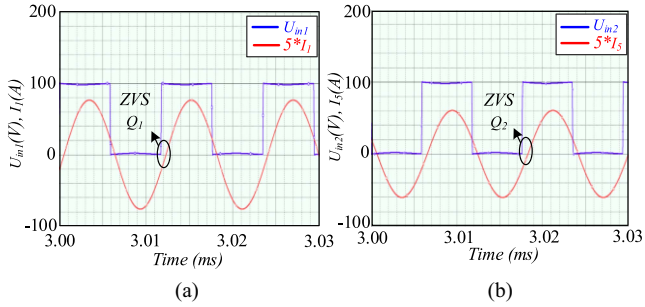

Fig. 9. Key waveforms at the coupling coefficient of 0.1. (a) $U_{\rm in1}$ and $I_{\rm in1}$. (b) $U_{\rm in2}$ and $I_{\rm in2}$.

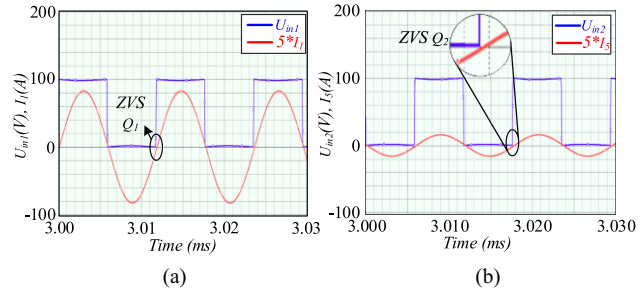

Fig. 10. Key waveforms at the coupling coefficient of 0.4. (a) $U_{\rm in1}$and $I_{\rm in1}$. (b) $U_{\rm in2}$ and $I_{\rm in2}$.

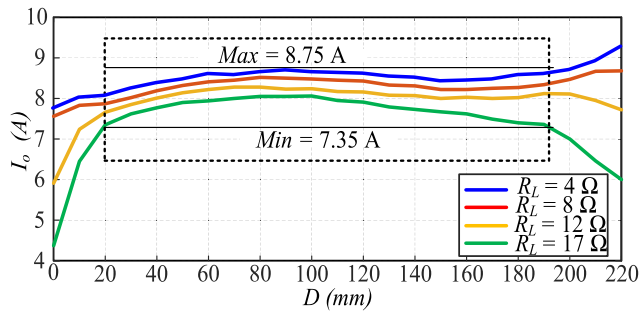

Fig. 11. Variations of the output current with respect to the distance between the magnetic couplers in different load resistances.

In Figs. 9 and 10, the output voltage of inverter at each resonance circuit, $U_{\rm in1}$ and $U_{\rm in2}$, and resonance currents, I_1 and I_5, are given for a 10 Ω load, with coupling coefficients from 0.1 to 0.4. A lower coupling coefficient (0.1, Fig. 9) increases the phase difference between inverter voltages and currents, while a higher coefficient (0.4, Fig. 10) reduces it, still achieving ZVS. Fig. 11 shows the output current changes with distance (0–220 mm) and load resistance (4 Ω to 17 Ω). The output current is approximately 8.05 A, peaking at 8.75 A and dropping to 7.35 A.

The percentage variation in output current for distances from 20 mm ($K_{L1L4} = 0.42$, $K_{L2L3} = 0.46$, $K_{L5L6} = 0.49$) to 190 mm ($K_{L1L4} = 0.113$, $K_{L2L3} = 0.122$, $K_{L5L6} = 0.121$) remains under 9% . Fig. 12 shows that across all distances, the output current stays between 7.35 A and 8.75 A, stabilizing around 8.05 A. While the current change rate is minimal up to 140 mm, it increases beyond 190 mm, limiting the topology's efficient performance.

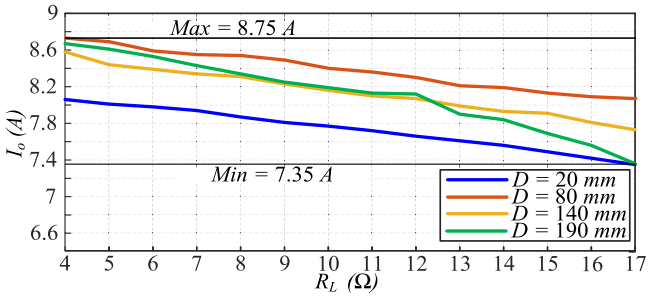

Fig. 12. Output current variations versus resistance at different magnetic coupler distances.

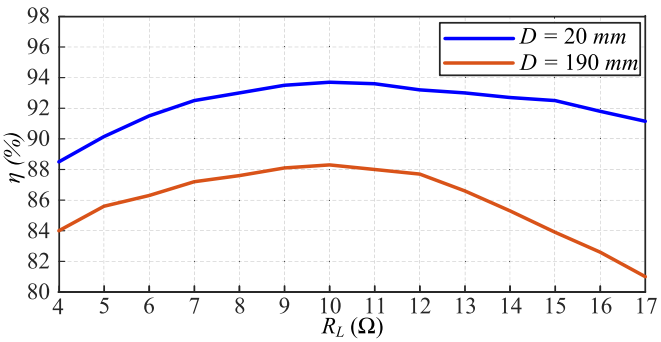

Fig. 13. Efficiency of the converter for two given distances.

Accordingly, the proposed magnetic coupler is capable of keeping regulated output current in various airgap values up to 190 mm, which the coupling coefficient of $K = 0.1$ yields. In Fig. 13, the system efficiency is presented relative to the load resistance at two different distances, minimum and maximum eligible amount. The highest system efficiency occurred at a load resistance of 10 Ω, reaching 93.7% at a distance of 20 mm and 88.3% at a distance of 190 mm. Simulation results show that converter's efficiency of the system ranges between 81% and 94%, with given input voltage of 100 V and different load resistances. Unlike conventional topologies where the optimal load varies with changes in the coupling coefficient, in this system, the optimal load is independent of the coupling coefficient. The optimal load remains consistently at 10 Ω for both distances of 20 mm and 190 mm.

V. Experimental Evaluation

To validate the proposed circuit's performance, a 1kW prototype of hybrid IPT topology was developed using DDQDD magnetic couplers on both the primary and secondary sides. Fig. 14 shows the primary magnetic coupler arrangement with coils L_1, L_2, and L_5. Coil L_2 is in a DD layout in the first layer, L_5 rotated 90° in the second layer, and square-shaped L_1 in the third layer, mirrored in the secondary pad. Molds with grooves for each coil were 3D-printed to improve wiring accuracy and reduce wire usage. The coils use Litz wire (100 strands, AWG29). Ferrite cores are arranged in a square lattice for both the primary and secondary couplers, which include DD coils L_3 and L_6 as well as square coil L_4. Fig. 15 shows the overall implemented system.

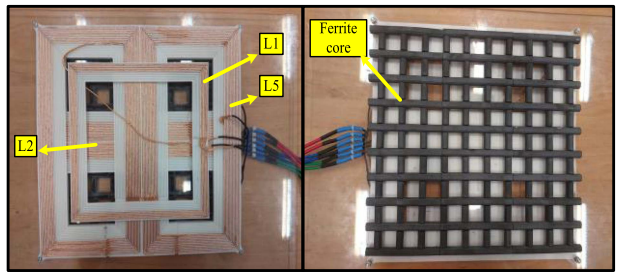

Fig. 14. Experimental magnetic coupler. (a) Front view of three-layer DDQDD. (b) Ferrite network of three-layer DDQDD (back view).

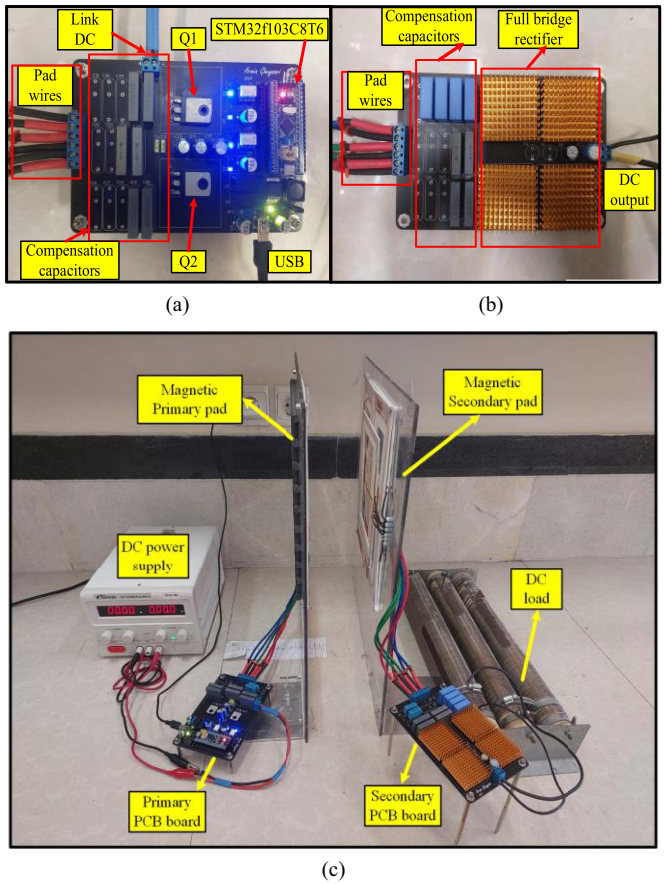

Fig. 15. Experimental setup including; (a) primary side's circuit, (b) secondary side's circuit, and (c) overall view of setup including electronic and magnetic part.

A compact PCB board on the primary side uses an affordable STM32F103C8T6 processor for pulse generation and MOSFET control. TLP350 gate drive ICs amplify and isolate the generated input pulses, with a USB jack embedded to power the gate drives and processor. Two MOSFETs serve as Q_1 and Q_2 switches, while MKP capacitors are used in the compensator circuits on both sides due to their precise capacitance and robustness against high-frequency voltage changes. The secondary side features a compact PCB with MKP capacitors and four Schottky diodes, along with two inexpensive 20 μF electrolytic capacitors for output filtering. A dc power supply of 100 V/10 A powers the circuit, with a simple heater as the dc load.

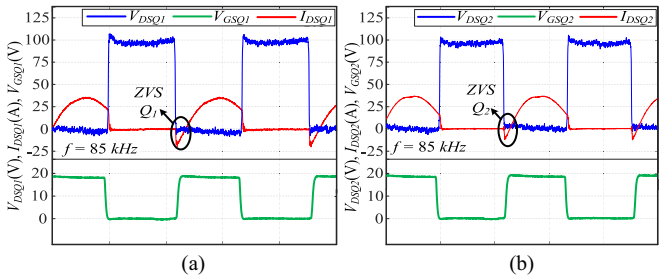

Fig. 16. Waveforms of drain-source voltage, gate-source voltage and drain-source current of MOSFETs. (a) Q_1, and (b) Q_2 at distance of 190 mm.

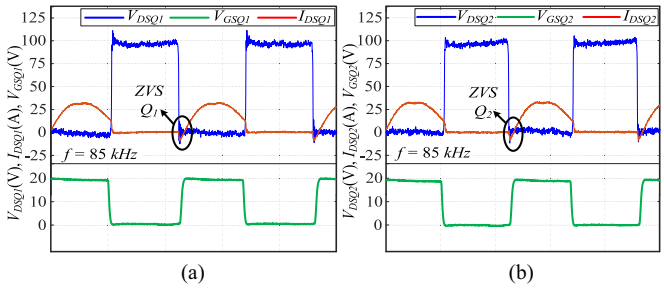

Fig. 17. Waveforms of drain-source voltage, gate-source voltage and drain-source current of MOSFETs. (a) Q_1, and (b) Q_2 at distance of 20 mm.

Figs. 16 and 17 show the drain-source (V_{DSQ}) and gate-source (V_{GSQ}) waveforms of MOSFETs Q_1 and Q_2 at 190 and 20 mm. Before V_{GSQ}, the body diode conducts, keeping V_{DSQ} at zero; applying V_{GSQ} achieves ZVS. Once V_{GSQ} is applied, the MOSFET turns ON, achieving soft switching (ZVS). Fig. 16(a) and (b) indicates that the equivalent impedance reflected to the primary side is inductive, as the inverter's output current leads the corresponding output voltage. Similar tests at different distances between magnetic couplers show comparable waveforms in Fig. 17 for a distance of 20 mm. Before applying V_{GSQ}, the body diode also conducts, resulting in zero voltage for the switch's drain-source. Applying V_{GSQ} achieves ZVS, and comparing Fig. 16(a) and (b) with Fig. 17(a) and (b) reveals that reducing the air gap decreases the phase difference between the inverter's voltage and current zero crossings, improving power factor from the inverter side.

Variations in output current concerning different distances between magnetic couplers can be observed in Fig. 18. Changing the air gap from 20 mm (where $K_{L1L4} = 0.42$) to 190 mm ($K_{L1L4} = 0.113$) shows that maximum output current occurs at $D = 80$ mm for $R_L = 4\,\Omega$, at 8.75 A. The minimum output current occurs at 190 mm and a load of 17 Ω, at 7.27 A, while output current remains almost constant at 8 A with only 9% tolerance. The small difference between experimental and simulated results is due to dissimilar shapes of ferrite cores in simulation (3-D finite element simulation in Maxwell) compared to actual materials (curvy shaped ferrites). In Fig. 19, variations in the output current of the circuit with respect to different load resistances at four different distances between magnetic couplers are presented. It is observed that the output current remains within the narrow band between 7.27 and 8.75 A for all distances, indicating a consistent performance. Specifically, at a distance of 20 mm, the output

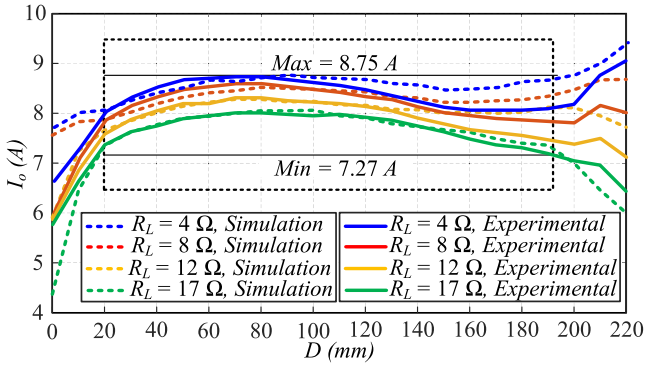

Fig. 18. Variations of the output current with respect to distances for different loads.

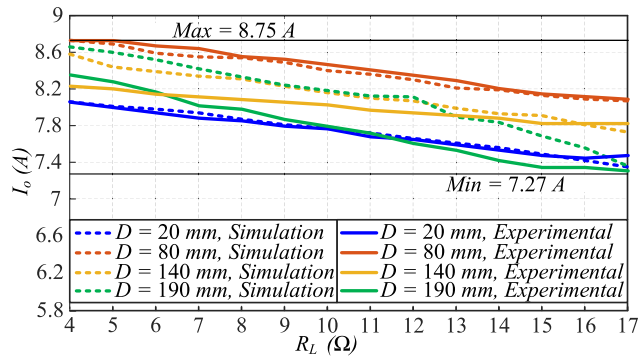

Fig. 19. Variations in the output current of the circuit versus load resistances for different distances.

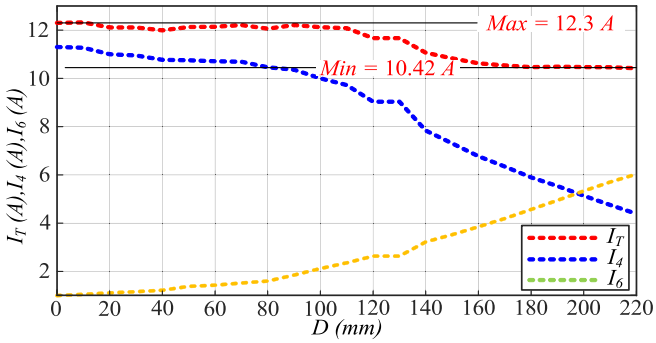

Fig. 20. Variations of the currents I_T, I_4, and I_6 with respect to distances for output load 10 Ω without considering coupling between L_1, L_4.

current curve in experiment is more aligned to the simulation result. However, as the distance increases, due to the scattering of magnetic flux at larger distances, discrepancy between the output current of the simulation and experimental results becomes more sensible, though both corresponding curves have similar trend.

Fig. 20 illustrates the variations of the RMS currents I_4, I_6, and I_T with respect to changes in the air gap distance between the magnetic couplers in the absence of coupling between inductors L_1 and L_4. In this case, the output current varies between 12.3 A and 10.42 A. In contrast, Fig. 21 shows the RMS current variations of I_4, I_6, and I_T under the same conditions, but with coupling present between inductors L_1 and L_4. Here, the output

TABLE II
COMPARISON WITH PREVIOUS SIMILAR WORKS

Reference	Number of S/D/L/CI/C	Coil structure	Output feature	Having AS switch or active rectifier	Output power	Maximum efficiency	varying airgap	Output oscillation	Sensitivity
Wang et al. [18]	8/4/2/4/6	BP	CC/CV	No	2 kW	92.1%	33.3%	10%	30%
Zhao et al. [19]	8/0/2/4/6	BP	CC	No	3.3 kW	91.6%	10%	NG	NG
Chen et al. [20]	8/4/4/4/8	DD-Q	CC/CV	No	1 kW	93.9%	33.3%	NG	NG
Qu et al. [21]	4/4/2/4/6	DD-Q	CC	No	3.5 kW	93.6%	15%	5%	33%
Zou et al. [22]	10/2/0/2/2	Circular	CP	Yes	500 W	93%	40%	NG	NG
Lu et al. [23]	4/4/3/2/4	Square	CV or CC	Yes	600 W	94.99%	10%	4.24%(CV) 5.63% (CC)	42.4%(CV) 56.3% (CC)
Zhao et al. [24]	4/4/1/4/5	BP	CV	Yes	3 kW	93%	22%	5%	22.7%
Wang et al. [25]	4/4/0/4/5	BP	CC	Yes	3.2 kW	96.7%	20%	5%	25%
Wang et al. [26]	4/4/1/3/4	CRSP	CV	No	1 kW	88%	12.5%	4.52%	36.1%
This article	2/4/0/6/6	DDQDD	CC	No	1 kW	92%	56.6%	9%	15.9%

Note: S, switch; D, diode; L, inductor; CI, coupled inductor; C, capacitor

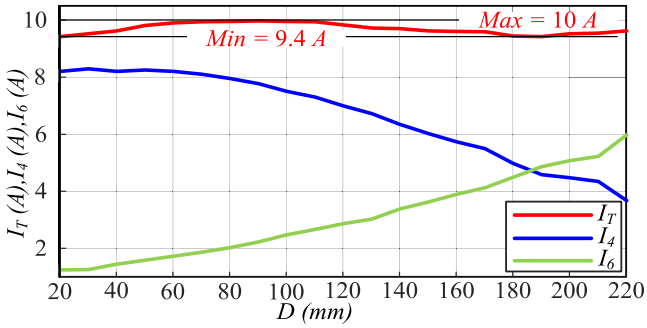

Fig. 21. Variations of the currents I_T, I_4, and I_6 with respect to distances for output load 10 Ω and coupling between L_1, L_4.

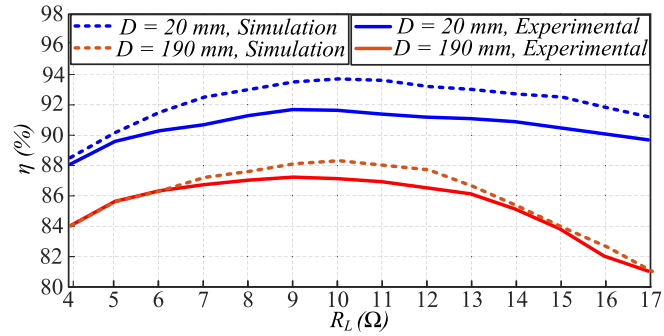

Fig. 23. DC–DC efficiency of the system in different loads for up and down limit value of distances ($D = 20$ mm and $D = 190$ mm).

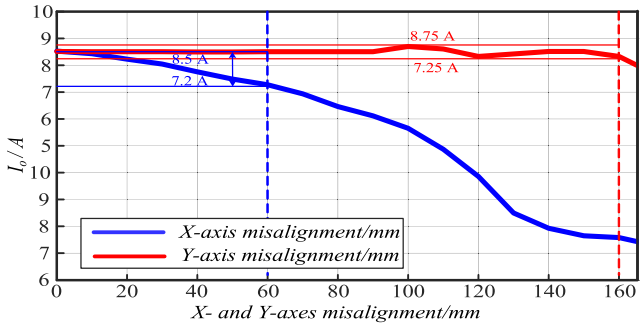

Fig. 22. Variations of the output current with respect to *X*- and *Y*-axes misalignment for output load 10 Ω.

current varies within a narrower range, from 10 to 9.4 A. As the air gap increases, current I_4 decreases while current I_6 increases, and the output current I_T remains almost constant. This balance between the two currents highlights the effect of the air gap on system performance, indicating a significant reduction in output current fluctuations, which is consistent with the expectations based on (7) and (8) discussed in Section II.

Similar experiments were conducted with misalignments along the x and y-axes, as illustrated in Fig. 22. The system demonstrated tolerance for misalignments of up to 60 mm along the *x*-axis (20% of the magnetic coil size) and 160 mm along the y-axis (53% of the magnetic coil size), with output current variations remaining below 9% in both cases. Although the system performs well under *x*- and *y*-axis misalignments, these aspects are not extensively investigated in this article. Instead, this article focuses on air gap variations caused by EVs' different ground clearances, aiming to address supriority of the proposed system for wide range of air gap distances.

Fig. 23 demonstrates the dc–dc efficiency variations across different loads at 20 and 190 mm air gaps. The circuit maintains 81–92% efficiency under all tested conditions. At 20mm gap, efficiency deviations between experiments and simulations become more noticeable due to ferrite core effects on winding self-inductance [see Fig. 7], which disturbs proper resonance and increases reactive current flow. Nevertheless, the maximum efficiency difference remains within 2%, showing excellent agreement. The system consistently achieves peak efficiency at 10 Ω load resistance in both simulations and experiments, proving a robust design without requiring coupling estimation.

The proposed WPT system outperforms nine prior studies in Table II, delivering a simpler, more robust solution for CC applications. With only two switches, four diodes, zero inductors, six couplers, and six capacitors, it reduces components compared to [18], [19], [20] and [22], which use 8–10 switches, significantly increasing control complexity and switching losses. Unlike [22], [23], [24], [25], this article avoids AS switches or active rectifiers, which were resulting in high ac voltage stress and control challenges, thereby reducing stability. At 1 kW, its 92% efficiency surpasses [26] (88%), while its 56.6% airgap

tolerance exceeds the 10% –40% of others. Output oscillation is low at 9%, and sensitivity defined as the ratio of output variation to airgap change is only 15.9%, outperforming all ([18], [19], [20], [21], [22], [23], [24], [25], [26]: 30%, NG, NG, 33%, NG, 42.4% –56.3%, 22.7%, 25%, 36.1%). This inherently low oscillation simplifies closed-loop control, aiming to eliminate complex methods. The DDQDD coil structure optimizes performance without extra inductors, unlike [20] and [23], cutting cost and interference. This design achieves an exceptional balance of simplicity and robustness, providing a 1 kW output with high stability and minimal sensitivity, marking a significant advancement over existing works and offering a practical, scalable solution for next-generation IPT charger with CC charging scenario. Due to the scalability of the proposed hybrid topology, it can also be used at higher power levels. By using SiC MOSFETs at higher power levels and maintaining ZVS under all coupling mismatches through the proposed method, the inverter can operate with low switching loss and robust performance. The voltage and current stresses across the resonant tank can also be mitigated through the series/parallel configuration of resonant capacitors and the optimum design of Litz wire used in magnetic couplers.

VI. Conclusion

This article introduces a new hybrid topology comprising *LCC* and Series compensation network in primary and secondary side as well as air-core inductive couplers between two side's compensator circuits to maintain a constant output current across varying loads and distances. The circuit is simplified to just two switches, reducing cost and complexity. A 1 kW experimental setup demonstrated that varying the load from 4 to 17 Ω and the distance between couplers from 20 mm to 190 mm results in an output current tolerance of less than 9% . Compared to existing hybrid IPT chargers, this system features fewer compensation elements, fewer switches, and improved tolerance to varying airgap from 33.3% in most relevant reference to 56.6% in this article. Additionally, the MOSFET switches operate under ZVS conditions, which lowers power losses and enhances efficiency.

References

[1] L. Wang et al., "Joint real-time identification for mutual inductance and load charging parameters of IPT system," *IEEE J. Emerg. Sel. Topics Power Electron.*, vol. 11, no. 4, pp. 4574–4590, Aug. 2023.

[2] Z. Zhang, H. Pang, A. Georgiadis, and C. Cecati, "Wireless power transfer—An overview," *IEEE Trans. Ind. Electron.*, vol. 66, no. 2, pp. 1044–1058, Feb. 2019.

[3] Y. C. Liu, J. Zhang, C. K. Tse, C. Zhu, and S.-C. Wong, "General pathways to higher order compensation circuits for IPT converters via sensitivity analysis," *IEEE Trans. Power Electron.*, vol. 36, no. 9, pp. 9897–9906, Sep. 2021.

[4] G. Li, H. Zhang, Y. Chen, J. Xie, C.-H. Jo, and D.-H. Kim, "3-D misalignment tolerant E-scooter IPT system with hybrid control based on three-coil design for load-independent CC/CV outputs," *IEEE Trans. Transp. Electrific.*, vol. 10, no. 4, pp. 9163–9177, Dec. 2024.

[5] M. J. Ebrahimi, A. Gheysari, M. A. Shamsi Nejad, and A. Y. Varjani, "An IPT system for stable output power transfer and efficiency improvement against large coupling variations," in *Proc. 16th Power Electron., Drive Syst., Technol. Conf.*, 2025, pp. 1–6.

[6] Z. Gong, Q. Shi, J. Li, and X. Tong, "Parallel hybrid wireless charging with misalignment tolerance and constant current output," in *Proc. Int. Conf. Mech. Electron. Eng.*, 2022.

[7] S. Bajelvand, A. Y. Varjani, S. Vaez-Zadeh, and A. Babaki, "Design of a high-efficient IPT system for battery charging under CP–CV charging scenarios," *IEEE Trans. Energy Convers.*, vol. 38, no. 3, pp. 1650–1658, 2023.

[8] V.-B. Vu et al., "Operation of inductive charging systems under misalignment conditions: A review for electric vehicles," *IEEE Trans. Transp. Electrific.*, vol. 9, no. 1, pp. 1857–1887, Mar. 2023.

[9] D. Patil, M. K. McDonough, J. M. Miller, B. Fahimi, and P. T. Balsara, "Wireless power transfer for vehicular applications: Overview and challenges," *IEEE Trans. Transp. Electrific.*, vol. 4, no. 1, pp. 3–37, Mar. 2018.

[10] Y. Zhang, Z. Huang, R. Xie, X. Chen, and Z. Li, "Misalignment tolerance and interoperability of wireless charging system based on two-channel topology and coil optimization," *IEEE Access*, vol. 12, pp. 120306–120315, 2024.

[11] J. Li, X. Zhang, and X. Tong, "Research and design of misalignment-tolerant LCC–LCC compensated IPT system with constant-current and constant-voltage output," *IEEE Trans. Power Electron.*, vol. 38, no. 1, pp. 1301–1313, Jan. 2023.

[12] G. Li and H. Ma, "A hybrid IPT system with high-misalignment tolerance and inherent CC–CV output characteristics for EVs charging applications," *IEEE J. Emerg. Sel. Topics Power Electron.*, vol. 10, no. 3, pp. 3152–3160, Jun. 2022.

[13] Z. Li, Q. Deng, S. Li, H. Deng, Q. Huang, and W. Hu, "LPV modeling and robust control of dynamic wireless charging for electric vehicles," *IEEE Trans. Ind. Electron.*, vol. 72, no. 10, pp. 10629–10639, Oct. 2025, doi: 10.1109/TIE.2025.3548993.

[14] Y. Zeng, Z. Shi, J. Wang, Z. Liu, and X. Li, "Virtual DC motor-based coordinated control strategy for multi-receiver dynamic WPT system," *IEEE Trans. Power Electron.*, vol. 40, no. 11, pp. 17503–17513, Nov. 2025, doi: 10.1109/TPEL.2025.3586221.

[15] T. Singhavilai, J. Tippayachai, K. Jirasereeamornkul, C. Ekkaravarodome, and T. Samanchuen, "Evaluating wireless power transfer technologies for electric vehicles: Efficiency and practical implementation of inductive, capacitive, and hybrid systems," *IEEE Access*, vol. 13, pp. 9792–9808, 2025.

[16] W. Xiong, Z. Yan, D. Tang, W. Zhou, and R. Mai, "A hybrid topology IPT system with partial power processing for CC–CV charging," *IEEE Trans. Power Electron.*, vol. 39, no. 1, pp. 1701–1712, Jan. 2024.

[17] S. Bajelvand, A. Babaki, A. Jafari-Natanzi, A. Y. Varjani, and S. Vaez-Zadeh, "A fixed-frequency control method for wireless power transmission battery chargers using a dual-function compensator," *IET Power Electron.*, vol. 17, no. 8, pp. 930–940, Jun. 2024.

[18] Y. Wang et al., "A misalignment-tolerant hybrid coupler for electric vehicle IPT charging systems," *IEEE Trans. Veh. Technol.*, vol. 72, no. 10, pp. 12845–12856, Oct. 2023.

[19] L. Zhao, D. J. Thrimawithana, and U. K. Madawala, "Hybrid bidirectional wireless EV charging system tolerant to pad misalignment," *IEEE Trans. Ind. Electron.*, vol. 64, no. 9, pp. 7079–7086, Sep. 2017.

[20] Y. Chen, B. Yang, Z. Kou, Z. He, G. Cao, and R. Mai, "Hybrid and reconfigurable IPT systems with high-misalignment tolerance for constant-current and constant-voltage battery charging," *IEEE Trans. Power Electron.*, vol. 33, no. 10, pp. 8259–8269, Oct. 2018.

[21] X. Qu, Y. Yao, D. Wang, S.-C. Wong, and C. K. Tse, "A family of hybrid IPT topologies with near load-independent output and high tolerance to pad misalignment," *IEEE Trans. Power Electron.*, vol. 35, no. 7, pp. 6867–6877, Jul. 2020.

[22] B. Zou, Z. Huang, I.-W. Iam, and C.-S. Lam, "Tuning control against coupler parameter variations due to misalignment in an optimal-efficiency-tracking and constant-power-output IPT system," *IEEE Trans. Power Electron.*, vol. 40, no. 5, pp. 7500–7511, May 2025.

[23] Y. Lu et al., "Design of compensation topology for IPT system considering coils' parameters and load variations for CC or CV output," *IEEE Trans. Transp. Electrific.*, vol. 10, no. 1, pp. 1583–1595, Mar. 2024.

[24] W. Zhao, X. Qu, J. Lian, and C. K. Tse, "A family of hybrid IPT couplers with high tolerance to pad misalignment," *IEEE Trans. Power Electron.*, vol. 37, no. 3, pp. 3617–3625, Mar. 2022.

[25] X. Wang, M. Leng, X. Zhang, Q. Tian, L. He, and H. Ma, "An intermediate coil for misalignment tolerant IPT system with dual decoupled receivers," in *Proc. 49th Annu. Conf. IEEE Ind. Electron. Soc.*, 2023, pp. 1–5.

[26] H. Wang, Y. Wu, Z. Shen, W. Pan, X. Chen, and Y. Zhang, "High-misalignment-tolerant dual-channel inductive power transfer system based on cross-shaped reversed-winding-incorporated solenoid pad," *IEEE Trans. Ind. Electron.*, vol. 71, no. 10, pp. 12499–12509, Oct. 2024.

Armin Gheysari (Student Member, IEEE) was born in Shahrekord, Iran, in 2000. He received the B.Sc. degree in power electrical engineering from Arak University, Arak, Iran, in 2022, and the M.Sc. degree in power electronics from the Tarbiat Modares University, Tehran, Iran, in 2025.

Since 2022, he has been a Research Assistant with the Industrial Electronics Laboratory, and Electrical Machines and Drives Laboratory, Tarbiat Modares University. His research interests include power electronics, inductive power transfer power electronic converter design, battery charger, and electric vehicles.

Ali Yazdian Varjani (Member, IEEE) received the B.Sc. degree in electrical engineering from the Sharif University of Technology, Tehran, Iran, in 1989, the M.Eng. and Ph.D. degrees in electrical engineering from the University of Wollongong, Wollongong, NSW, Australia, in 1995 and 1999, respectively.

Since 1999, he has been with Tarbiat Modares University, Tehran, Iran, where he is currently an Associate Professor with Power Electronics Department and the Director of the Industrial Electronics Laboratory, Electrical Machines and Drives Laboratory, and Cyber Physical Energy Systems Laboratory. His current research interests include a variety of research issues associated with topics related to information and communication technology and industrial electronics.

Amir Babaki (Member, IEEE) received the B.Sc. and M.Sc. degrees in electrical engineering and the Ph.D. degree in power electronics from the University of Tehran, Tehran, Iran, in 2012, 2014, and 2020, respectively.

During his Ph.D., he has been active as a Visiting Researcher with the IPT Group, University of Auckland, New Zealand. Since 2022, he has been a Postdoc with the Center for Industrial Electronics (CIE), University of Southern Denmark, Denmark, where he was engaged in the prestigious Danish EUDP project. He is currently an Assistant Professor of power electronics with CIE. His research interests include inductive power transfer, active front end converter, high speed power converter and electric vehicle.